Numerical Simulation of the Freeze-Thaw Behavior of Mortar Containing Deicing Salt Solution

Hadi S. Esmaeeli[1], Yaghoob Farnam[1], Dale P. Bentz[2], Pablo D. Zavattieri[1], and Jason Weiss[3,*]

[1] Lyles School of Civil Engineering, Purdue University, 550 Stadium Mall Dr., West Lafayette, IN 47907, USA

[2] Materials and Structural Systems Division, National Institute of Standards and Technology, 100 Bureau Dr., Stop 8615, Gaithersburg, MD 20899, USA

[3] School of Civil & Construction Engineering, Oregon State University, 111 Kearney Hall, Corvallis, OR 97331, USA

ABSTRACT

This paper presents a one-dimensional finite difference model that is developed to describe the freeze-thaw behavior of an air-entrained mortar containing deicing salt solution. A phenomenological model is used to predict the temperature and the heat flow for mortar specimens during cooling and heating. Phase transformations associated with the freezing/melting of water/ice or transition of the eutectic solution from liquid to solid are included in this phenomenological model. The lever rule is used to calculate the quantity of solution that undergoes the phase transformation, thereby simulating the energy released/absorbed during phase transformation. Undercooling and pore size effects are considered in the numerical model. To investigate the effect of pore size distribution, this distribution is considered using the Gibbs-Thomson equation in a saturated mortar specimen. For an air-entrained mortar, the impact of considering pore size (and curvature) on freezing was relatively insignificant; however the impact of pore size is much more significant during melting. The fluid inside pores smaller than 5 nm (i.e., gel pores) has a relatively small contribution in the

* Corresponding author: W. Jason Weiss, jason.weiss@oregonstate.edu

26 macroscopic freeze-thaw behavior of mortar specimens within the temperature range used in this

27 study (i.e., +24 °C to -35 °C), and can therefore be neglected for the macroscopic freeze-thaw

28 simulations. A heat sink term is utilized to simulate the heat dissipation during phase

29 transformations. Data from experiments performed using a low-temperature longitudinal guarded

30 comparative calorimeter (LGCC) on mortar specimens fully saturated with various concentration

31 NaCl solutions or partially saturated with water is compared to the numerical results and a

32 promising agreement is generally obtained.

33   Keywords: Degree of saturation, deicing salt, finite difference method, freeze and thaw,

34 cementitious, pore size distribution, undercooling.

35 **1. Introduction**

36   Deicing salts are applied to the surface of concrete pavements to melt ice and snow in an

37 effort to improve safety conditions for the traveling public. The solution that is produced (e.g.,

38 water-NaCl, $CaCl_2$, $MgCl_2$) can be absorbed into concrete pores. This solution alters the degree

39 of saturation (i.e., the volume ratio of fluid in the specimen as compared to the total maximum

40 volume of fluid that the specimen can hold) of the concrete pavement, the freezing temperature

41 of the solution within the concrete pores, and the damage that may result [1−13].

42   Prediction of phase transformation within the pores requires an understanding of heat flow

43 within a mortar during a freezing/thawing cycle [14, 15]. For the purpose of this discussion, the

44 term "latent heat" is used to denote the amount of energy released or absorbed during a phase

45 transformation (formation or melting of ice or eutectic solid). The latent heat produced by the

46 phase transformation of the pore solution can be used to quantify the amount of pore solution in

47 concrete that freezes [2]. There are two main phenomena that affect the freezing of pore solution

48 in a mortar/concrete: (1) its pore size distribution and (2) undercooling, as described below.

49 First, the pore size distribution in concrete influences its freezing. Concrete pores are typically

50 categorized into three main classes: 1) gel pores with a radius smaller than 5 nm that are

51 associated with the formation of cement (binder) hydration products, 2) capillary pores that are

52 the remnants of the original water-filled space between (cement) particles and commonly range

53 from 5 nm to 5 µm in radius, and 3) pores (voids) associated with entrained or entrapped air that

54 range from 5 µm to 10 mm [16–19]. The size of the pores in the concrete can influence the

55 temperature at which freezing occurs. This is described using the Gibbs-Thomson equation [20].

56 A large fraction of water associated with pore sizes greater than 5 nm (i.e., capillary pores or

57 pores associated with entrained or entrapped air) is susceptible to freezing at a temperature above

58 -10 °C [9, 21, 22]. According to the Gibbs-Thomson equation, the water absorbed in the gel

59 pores will not begin to freeze until the temperature of the specimen drops to about -13 °C [22–

60 24]. It is also worth mentioning that the solution inside concrete pores (i.e., pore solution)

61 contains different ionic species (such as Na^+, K^+, Ca^{++}, and OH^-) [25] that depress its freezing

62 temperature [7]. The absorption of salt solution into the pores can further depress the freezing

63 temperature of this pore solution, due to the presence of additional ions such as Cl^- [5, 26, 27].

64 Undercooling also influences freezing in concrete. While it is expected that a solution freezes

65 at its characteristic melting point temperature, T_m, freezing usually occurs at a temperature (i.e.,

66 T_f) lower than T_m. This reduction in freezing temperature is known as undercooling [28–30] and

67 is primarily due to the fact that solidification (in most cases) requires the presence or formation

68 of nuclei that can trigger the freezing action. Once the heterogeneous nuclei are present in the

69 liquid phase, ice crystals begin to nucleate/grow and consequently the latent heat of fusion is

70   released into the undercooled liquid, increasing the temperature of the liquid toward T_m. Growth

71   of ice continues until the temperature of the liquid reaches T_m [28]. Afterwards, the temperature

72   of the liquid remains at T_m until the entire liquid solidifies, this is known as thermal arrest [28].

73   After thermal arrest, the amount of ice increases gradually as the temperature further decreases.

74   Melting however occurs gradually in the pores as the temperature of each pore reaches its T_m

75   value [9, 24, 31]. The amount of ice transformed to solution increases gradually as each set of

76   larger pores in turn reach the associated T_m (according to the Gibbs-Thomson equation) [24, 32].

77   These two phenomena (i.e., pore size and undercooling) affect the freezing behavior of pore

78   solution simultaneously in the mortar specimen and it may be essential to consider both in the

79   simulation during freezing. In melting, however, only pore size influences the thawing behavior.

80   Numerically, it is feasible to develop a theoretical model based on the heat transfer formulation

81   to predict and simulate phase transformation and heat transfer in materials [33, 34]. One-

82   dimensional finite difference [34–38], two-dimensional finite difference [34, 36, 38–40], control

83   volume [41–44], and finite element [45–47] based methods all have been used to simulate such

84   heat transfer problems. In this paper, a one-dimensional finite difference model is used. In

85   particular, this numerical method approximates the complex solid-liquid interactions in the

86   porous mortar using a fixed grid method [48, 49]. The computational model is applied to

87   estimate the thermal behavior of mortar containing NaCl solutions or just water under freeze-

88   thaw cycles. The formation of ice is quantified by calculating the volume fraction of ice that is

89   produced and the concentration of the remaining fraction of solution during cooling using the

90   lever rule [50, 51]. As the ice grows, the liquid to solid phase transformation releases latent

91   heat, ΔH_f , that increases the temperature of the material locally and slows down the ice growth.

92   An empirical approach is used to account for the sudden latent heat release produced by

93   undercooling. This model is also used to describe, analyze and interpret the experimental data

94   obtained from low-temperature longitudinal guarded comparative calorimeter (LGCC) tests

95   [9,11].

96   **2. Numerical simulation**

97   The main objective of this study is to predict the thermal response of a mortar (considered at a

98   macroscopic scale) that is experiencing phase transformations during a reduction and subsequent

99   increase in specimen temperature (i.e., a freezing and thawing cycle). The goal of the simulations

100   is to quantify the fraction of pore solution that can freeze in an undercooled mortar specimen.

101   The temperature of the specimen can be tracked by solving the heat (energy balance) equation

102   and considering the frozen fraction of the pore solution. The governing equation for the heat

103   transfer within a mortar specimen can be described using the energy balance Equation 1 [54].

$$\frac{\partial}{\partial x}\left[k_m(T)\cdot\frac{\partial T(x,t)}{\partial x}\right]+q_{gen}-q_{loss}=\rho_m(T)\cdot C_m^p(T)\cdot\frac{\partial T(x,t)}{\partial t} \qquad \mathbf{1}$$

104   where $T(x,t)$ is the temperature at location $x(mm)$ and time $t(\sec)$, $k_m(T)$ is the thermal

105   conductivity of the mortar specimen $[W/(m\cdot K)]$ at temperature T, $\rho_m(T)$ is the density of the

106   mortar specimen $\left(kg/m^3\right)$ at temperature T, C_m^p is its specific heat capacity $[J/(kg\cdot K)]$ at

107   temperature T, q_{gen} is the rate of generated or consumed heat from any phase change of the

108   pore solution $\left[J/\left(m^3\cdot\sec\right)\right]$, and q_{loss} is the rate of heat dissipation (to the environment) in the

109   experiment $\left[J/\left(m^3\cdot\sec\right)\right]$.

110   In Equation 2a, the incorporation of a released/absorbed latent heat term, q_{gen} associated

111   with freezing/melting of the pore solution within a mortar specimen is described. A heat sink

112   term, q_{loss} is also included as shown in Equation 2b to calculate the rate of heat dissipation to

113   the environment (even though insulation is present). This heat term is considered as a fraction of

114   the rate of generated latent heat to simulate the significant heat exchange between the mortar

115   specimen and its surroundings in the lateral directions.

$$q_{gen} = \Delta H_f \cdot \rho_{so\ln} \cdot v_P \cdot \frac{\partial[v_F(T) \cdot \xi(T)]}{\partial t} \qquad \textbf{2a}$$

$$q_{loss} = \Delta H_f \cdot h_{loss} \cdot \rho_{so\ln} \cdot v_P \cdot \frac{\partial[v_F(T) \cdot \xi(T)]}{\partial t} \qquad \textbf{2b}$$

$$q_{gen} - q_{loss} = \Delta H^m_f \cdot \rho_{so\ln} \cdot v_P \cdot \frac{\partial[v_F(T) \cdot \xi(T)]}{\partial t} \qquad \textbf{2c}$$

116   where ΔH_f is the latent heat of fusion (kJ/kg), $\rho_{so\ln}$ is the density of pore solution $\left(kg/m^3\right)$,

117   v_p is the total volume fraction of pores within the mortar specimen (0 to 1), $v_F(T)$ is the

118   volume fraction of the pore solution that can freeze at temperature T (0 to 1), $\xi(T)$ is the frozen

119   volume fraction of freezable pore solution with salt at temperature T (0 to 1), h_{loss} is the heat

120   dissipation coefficient (< 1), and $\Delta H^m_f = \Delta H_f \cdot (1 - h_{loss})$ is the apparent latent heat measured

121   considering heat dissipation during phase transformation in the system (< ΔH_f).

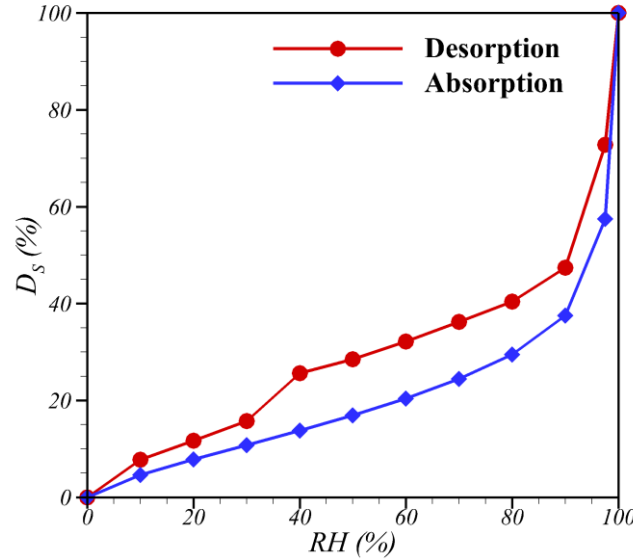122   **3. Frozen fraction of pore solution without salt, $v_F(T)$**

123   The mortar specimens contain a pore structure with a broad range of sizes. The pore size can

124   alter the freezing temperature of water [5–7, 27]. To determine the pore size distribution in the

125   mortar specimen and thus to calculate $v_F(T)$, a desorption isotherm was obtained for the mortar

126   using a dynamic vapor sorption analyzer (TA Q5000). The vacuum saturation method is used to

127   fully saturate the mortar specimen (i.e., D_S = 100 %). Therefore, all of the pores, including air

128   voids, are filled with water, to investigate the role of curvature of the pores on the thermal

129   behavior of the mortar. For melting, the pore size distribution obtained from an absorption

130   isotherm is used [55]. Figure 1 provides the desorption-absorption isotherm for the mortar

131   specimen and it correlates the degree of saturation (D_s) to the relative humidity (RH), which is

132   the amount of water vapor present in the specimen expressed as a percentage of the amount

133   needed for saturation at the same temperature [10]. A characteristic hysteresis is observed in the

134   absorption/desorption isotherm in Figure 1, at least partially due to the presence of "ink-bottle"

135   pores.

136   To calculate $v_F(T)$, two approaches were evaluated in this study: (1) a model with explicit

137   consideration of a continuous pore size distribution, and (2) a phenomenological model with

138   consideration of only a discrete pore size distribution. The first approach considers the effect of

139   all pore sizes on the freezing process and $v_F(T)$ varies continuously as the temperature

140   changes. In the second approach, the effect of a discrete pore size distribution on ice formation

141   inside the mortar specimen is simplified and a phenomenological model is adapted to simulate

142   the freezing process of water inside the mortar specimen (it considers only two classes of pores-

143   large pores that include all pores except gel pores (the capillary and air entrained/entrapped

144   pores) and small pores (known as gel pores)).

145   In the phenomenological model, $v_F(T)$ is considered to be a constant value based on three

146   main classes of pores: 1) gel pores, 2) capillary pores, and 3) water-filled pores associated with

147   entrained or entrapped air. To investigate the accuracy of these two approaches, the LGCC test

148   conducted by Farnam et al. [9, 11] was simulated using these two models with consideration of

149   continuous and discrete pore sizes, respectively, and also the thermal behavior of the mortar

150   specimens saturated with water was compared with experimental results obtained in a

151   temperature range between 24 °C and -35 °C.

Figure 1 Desorption-absorption isotherms of mortar specimen.

152   *3.1. A model with consideration of a continuous pore size distribution*

153   Equation 3 describes the Gibbs-Thomson equation that relates the freezing temperature of a

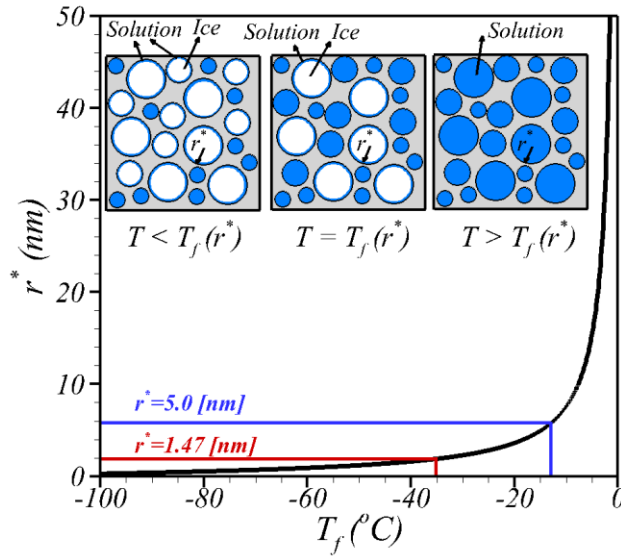154   liquid inside a porous material to the pore radius.

$$\frac{2\gamma_{CL}}{r^*} \approx \left(\frac{S_L - S_C}{V_L}\right)\left(T_m - T_f\left(r^*\right)\right)$$ **3**

155   where γ_{CL} is the crystal/liquid interfacial energy $\left(J/m^2\right)$, r^* is the radius of the pore for

156   homogeneous nucleation (m), S_L and S_C are the molar entropies of the liquid and crystalline

157   phases $[J/(mol \cdot K)]$, V_L is the molar volume of the liquid $\left(m^3/mol\right)$, T_m is the melting

158   temperature (K), and T_f is the freezing temperature as a function of pore radius (K)[24, 56].

159   Therefore, the temperature at which ice begins to form can be predicted as a function of critical

160   pore radius r^* by solving Equation 3 for T_f [20, 24, 32].

161   Figure 2 displays the relationship between the size of the pore and the temperature that is

162   needed to freeze water inside the pore, $T_f\left(r^*\right)$. At a temperature above $T_f\left(r^*\right)$, no phase

163   transformation occurs inside the pores with radius less than r^*. Once the temperature reaches the

164   associated freezing temperature, ice begins to form inside the pores with radii of r^*. Afterwards,

165   ice propagates into the smaller pores, but only as the temperature drops further. This process is
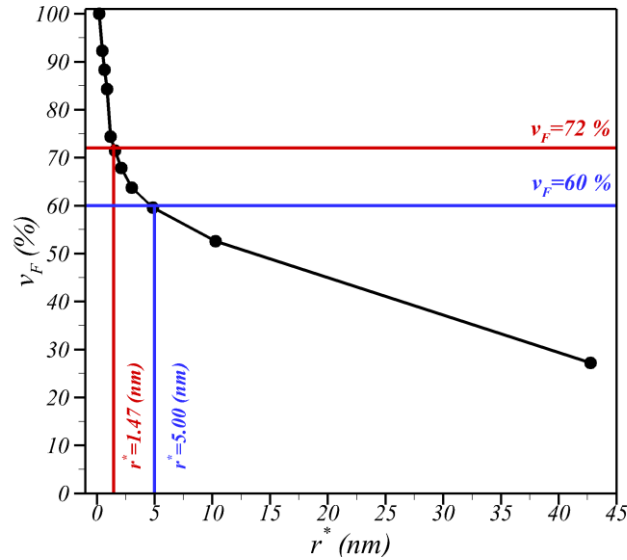
166   reversed during melting.

Figure 2 The effect of pore size on the freezing temperature of water using the Gibbs-Thomson equation, including a schematic of ice formation in a porous material (inset).

167   The Kelvin-Young-Laplace equation can be used to correlate the pore radius to the relative

168   humidity $\left(RH\right)$ in a water-filled pore as described in Equation 4 [57, 58].

$$r^* = \left(\frac{2\gamma}{\ln(RH)}\right)\cdot\left(\frac{V_m}{RT}\right)$$ **4**

169   In this study, the Kelvin-Young-Laplace equation (Equation 4) was used alongside the Gibbs-

170   Thomson equation (Equation 3) to obtain the relationship between $v_F(T)$ and pore size in the

171   mortar specimen based on its measured desorption isotherm (Figure 1). At a temperature of

172   -35 °C, solution absorbed into the mortar pores with sizes greater than 1.47 nm is susceptible to

173   freezing as shown in Figure 2. Figure 2 also displays the process of ice formation in a porous

174   material, as the ice forms inside the larger pores initially. Ice invades into the smaller pores

175   progressively as the temperature drops. Figure 3 shows that 72 % of the solution absorbed in the

176   pores by volume can freeze between 0 °C and -35 °C. For the case of melting, the formed ice in

177   the pores is similarly considered to melt gradually according to the Gibbs-Thomson equation

178   (Equation 3). In this work, it is assumed that $1 = v_{air} + (D_S/100)$ and

179    $(D_s/100) = v_w(r < r^*) + v_F(r > r^*)$ where v_{air} and v_w are the volume fraction of air and non-

180   freezable pore solution in the total pores (0 to 1), respectively. To investigate the role of pore

181   sizes, all of the pores with various sizes are assumed to be filled with water in this section, i.e.,

182    $v_{air} = 0$. It should be mentioned that the LGCC test was conducted within a temperature range

183   between 24 °C and -35 °C.

Figure 3 Volume fraction of pore solution that can freeze as a function of the critical nucleus (pore) size.

184   *3.2. A phenomenological model with consideration of a discrete pore size distribution*

185   Although the continuous pore size distribution can be estimated to determine the volume

186   fraction of freezable pore solution, this measurement is generally not available for

187   field/commercial concretes. In this paper, a phenomenological model is developed to use in

188   practice, when knowledge of the continuous pore size distribution is not available. Since the

189   freezing and thawing responses of most cementitious systems are dominated by the category of

190   relatively large pores (i.e., capillary, air-entrained, and air-entrapped pores), a discrete pore size

191   of 5 nm (a pre-defined critical pore size as the division between gel and capillary pores) can be

192   utilized as a criterion to differentiate the freezable and non-freezable pore solution [16, 21, 59].

193   For a mortar sample saturated with deionized water, this critical pore radius corresponds to a

194   relative humidity (RH) equal to 81 %, at which point all of the gel pores are filled by

195   solution [57].

196   The corresponding freezing temperature of water in pores with a size of 5 nm is about -13 °C

197   according to the Gibbs-Thomson equation as displayed in Figure 2. Figure 3 displays the relation

198   between derived volume fraction of freezable pore solution, v_F from associated relative

199   humidity measured in experiments, and pore radius, r^*, using equation 4. The corresponding

200   volume fraction of freezable pore solution, v_F, in pores with size greater than 5 nm is measured

201   to be 60 % with respect to the total volume fraction of pores displayed in this figure.

202   Consequently, the volume of freezable pore solution in the phenomenological model is

203   underestimated by about 16 % with respect to the model with direct consideration of pore size

204   distribution assuming pure water to be the solution in the pores. This implies that 60 % of the

205   total solution by volume, corresponding to the solution that is absorbed into large pores (i.e.,

206   capillary pores, air-entrained pores, and air-entrapped pores) begins to transform to ice

207   instantaneously and the gradual process of ice formation in the remainder of the freezable pores

208   (i.e., smaller pores, containing a lower volume fraction) will be neglected. Therefore, the radius

209   of curvature (pore size) would have a relatively small impact on the macroscopic freezing

210   response of the air-entrained mortar specimen and the approach of a discrete pore size

211   distribution will be implemented in the numerical model to investigate the thermal behavior of

212   mortar specimens containing NaCl solutions.

213   **4. Frozen fraction of pore solution with salt, $\xi(T)$**

214   For the case where the pores are water-filled (0 % NaCl), the value of $v_F(T)$ can be used to

215   determine the latent heat released/absorbed when the temperature of the specimen reaches

216   freezing/melting temperatures. In the case where the pores are filled with NaCl solution, the

217   presence of this salt alters the freezing/melting behavior. The phase equilibrium of NaCl solution

218   is shown in Figure 4. In this figure, the liquidus line shows the point at which ice begins to form

219   within the NaCl solution. Above the liquidus line, no ice may be detected (i.e., point 1 in Figure

220   4). A mixture of ice and salt solution with varying concentration that follows the liquidus line

221   exists between the liquidus and eutectic temperatures (T_{eut}= -21.1 °C), which is commonly

222   known as the freezing region (i.e., point 2). At T_{eut} (i.e., the eutectic line), the formation of ice is

223   complete and all the solution converts to a solid eutectic composition as the temperature of the

224   solution decreases further, which is described in more detail in section 8.2. Below this

225   temperature, it is assumed that no solution exists in the capillary, air-entrained and air-entrapped

226   pores. According to solidification principles [28], the lever rule can be used to determine the

227   amount of ice when the specimen temperature is between the liquidus and eutectic lines.

228   The frozen fraction of the freezable pore solution $\xi(T)$ was used in the numerical simulation

229   to calculate the amount of latent heat released/absorbed during freezing/melting at each time step

230   for the mortar specimen saturated with NaCl solution. The lever rule, given in Equation 5, was

231   employed in this study as a tool to compute the amount of produced ice within the freezing

232   region for NaCl solutions in a mortar specimen.

$$\xi(T) = \frac{c_s(T) - c_0}{c_s(T)} \qquad\qquad \textbf{5}$$

233   where $c_s(T)$, the concentration of the ice solution mixture, can be estimated as a function of

234   solution temperature by using Equation 6 [11]:

$$c_s(T) = a_2 \times T^2(x,t) + a_1 \times T(x,t) + a_0 \qquad -35^o C \leq T(x,t) \leq 24^o C \qquad \textbf{6}$$

235   where a_0=0.003385, a_1=-0.016362 [1/(°C)], a_2=-0.000264 [1/(°C^2)], and c_0 is the initial

236   concentration of NaCl solution above the liquidus line by mass (%). The coefficients in Equation

237   6 fit the $c_s(T)$ curve on data points derived from the phase diagram of aqueous NaCl solutions

238   with R^2=0.999 as the measure of goodness-of-fit.

239   The frozen fraction of the freezable pore solution $\xi(T)$ was calculated for bulk solutions

240   containing 0 %, 5 %, 10 %, and 23.3 % NaCl (by mass) and is depicted in Figure 4. This figure is

241   divided into three temperature ranges for solution with NaCl concentrations of 0 %, 5 %, 10 %,

242   and 23.3 % : (1) -35 °C $\leq T(x,t) \leq$ -21.1 °C $= T_{eut}$ where the temperature of solution is below T_{eut}

243   and the entire solution solidifies; (2) -21.1 °C $\leq T(x,t) \leq 0$ °C where both liquid and solid phases

244   (i.e., ice and solution) coexist; (3) 0 °C $< T(x,t) \leq 24$ °C where no phase transformation occurs

245   and the solution remains in its liquid state.

246   Ice formation or solidification of eutectic composition requires removal of sufficient

247   heat/energy to compensate for the latent heat associated with the phase transformation. A

248   considerable amount of latent heat can be released during solidification. Eutectic latent heat for

249   NaCl solution was measured using a low-temperature differential scanning calorimeter and

250   obtained to be $\Delta H_{eut}=$ 135 kJ/kg $\pm$ 5 kJ/kg. The standard deviation for eutectic latent heat was

251   determined on three mortar specimens containing NaCl solution with 5 %, 10 %, and 23.3 %

252   NaCl concentrations. The latent heat associated with ice formation was also considered to be

253    $\Delta H_{ice}=$ 332.4 kJ/kg $\pm$ 2 kJ/kg over the range of -35 °C $\leq T(x,t) \leq 0$ [14, 24, 56]. The heat of fusion

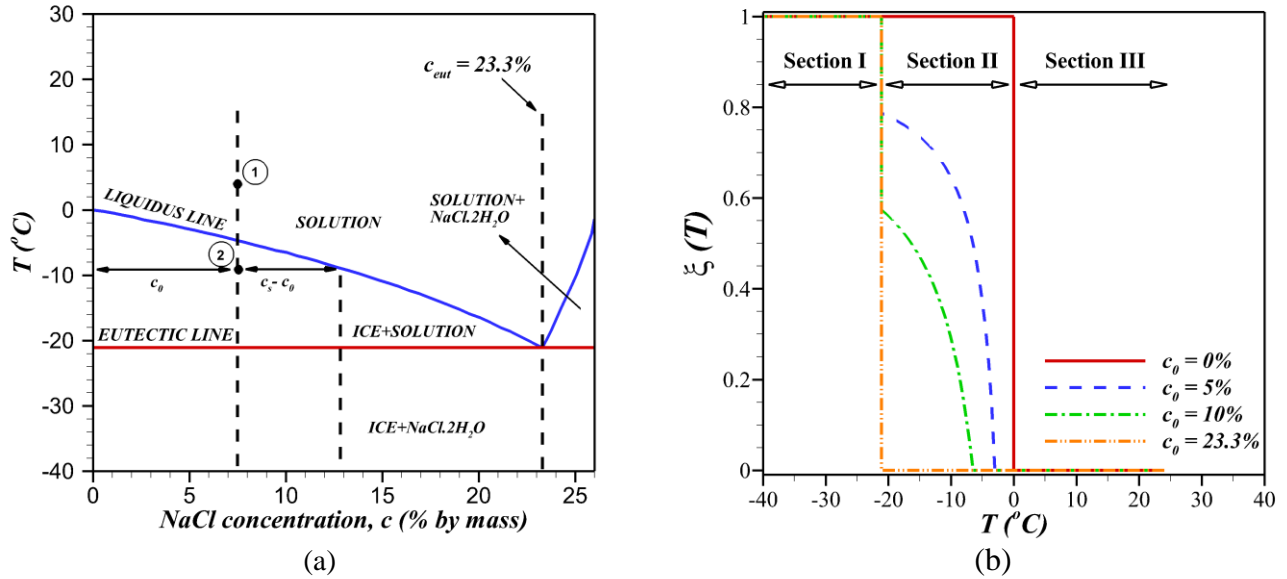254 $\Delta H_{melting}$ was given with a relative error < 0.25 % by Equation 7 [24]:

$$\Delta H_{melting}(T)(kJ/kg) \approx 333.8(kJ/kg) + 1.79[kJ/(kg \cdot K)] \cdot (T - T_m)\qquad \textbf{7}$$

255   The rate of ice formation within mortar pores was considered in the numerical simulation by

256   evaluating $\xi(T)$.

257   **5. Effective thermal properties of mortar specimen**

258   To develop a reliable numerical simulation at the macro-scale, it is essential to properly define

259   the material properties. This section discusses how the thermal properties of the mortar specimen

260   as a composite are defined for the proposed finite difference model with the consideration of two

261   approaches concerning the distribution of pore sizes, namely continuous and discrete.

Figure 4 (a) Phase diagram for aqueous NaCl solution [60]; (b) the fraction of produced ice as a function of temperature within the freezing region for bulk NaCl solution.

262   *5.1. Thermal Conductivity*

263   The effective medium theory (EMT) [61] can be used to define properties of a composite

264   material for a heterogeneous mixture. For mortar specimens either partially or fully saturated

265   with water or fully saturated with NaCl solution at different concentrations, the thermal

266   conductivity of the mortar (k_m) was estimated using the EMT formulation as described in

267   Equation 8 and shown in Figure 5a:

$$k_m = k_{dry} \cdot \frac{2(1-v_P) \cdot k_{dry} + (1+2v_P) \cdot k_P}{(2+v_P) \cdot k_{dry} + (1-v_p) \cdot k_P}$$ **8**

268   where k_{dry} is the thermal conductivity of the dry mortar specimen, k_p is the thermal

269   conductivity of the material in the pores, and v_p is again the total volume fraction of pores.

270   Depending on the temperature and saturation state, pores in the mortar specimen may contain

271   various constituents including air, ice, or NaCl solutions with different concentrations. The

272   amount of solution and air in the mortar depends on its degree of saturation (D_S). The

273   temperature of the mortar specimen can also change the amount of solution and ice in mortar

274   pores as described in sections 3 and 4. The change in the amount of air, ice, or solution can

275   substantially alter the thermal conductivity of the mortar specimen due to the considerable

276   differences between the thermal conductivities of air, solid ice, and solution (Table 1).

277   A parallel model [62] was employed to determine the effective k_P as a function of the volume

278   fractions and thermal conductivities of each component (i.e., k_{air}, k_{ice}, and $k_{so\ln}$), as described

279   in Equation 9.

$$k_P = k_{air} \cdot v_{air} + v_f \cdot \left[k_{ice} \cdot \xi + (1-\xi)k_{so\ln}\right] + k_{so\ln} \cdot v_w \qquad \mathbf{9}$$

280   where k_{air} is the thermal conductivity of air, $v_{air} = 1 - (D_S/100)$ is the volume fraction of air in

281   the mortar pores, k_{ice} is the thermal conductivity of ice, and $k_{so\ln}$ is the thermal conductivity of

282   the remnant pore solution within the mortar pores. Following the work of Farnam [9], no

283   considerable changes of dimensions of the mortar specimens were observed. Therefore, the

284   volume change is neglected in the thermal modeling of a macro-scale mortar specimen

285   ($v_{air} = 1 - (D_S/100)$). However, the variation of physical and thermal properties of components

286   of the mortar specimen may lead to a change in the volume of a micro-scale specimen.

287   It is worth mentioning that the unfrozen solution may exist in (1) smaller pores with an

288   invariable NaCl concentration, and (2) larger pores which contain frozen solution (ice) and a

289   NaCl solution with a higher concentration. The thermal properties of NaCl solution in the

290   smaller pores are provided in Table 1; however, the thermal properties of NaCl solution with

291 variable concentration in the larger pores can be determined knowing the frozen fraction and the

292 Lever rule. The corresponding thermal conductivities of air, ice, NaCl solution with different

293 concentrations, and dry mortar are also provided in Table 1.

294 *5.2 Density, ρ*

295 The law of mixtures (a weighted mean) can be used to predict the density of a composite

296 material. An effective density for mortar specimens $\left(\rho_m\right)$ was estimated using the law of

297 mixtures and is described in Equation 10 and shown in Figure 5b.

$$\rho_m = \rho_{dry} \cdot \left(1 - v_P\right) + \rho_P \cdot v_P$$

10

298 where ρ_{dry} is the density of the dry mortar and ρ_P is the effective density of the materials in

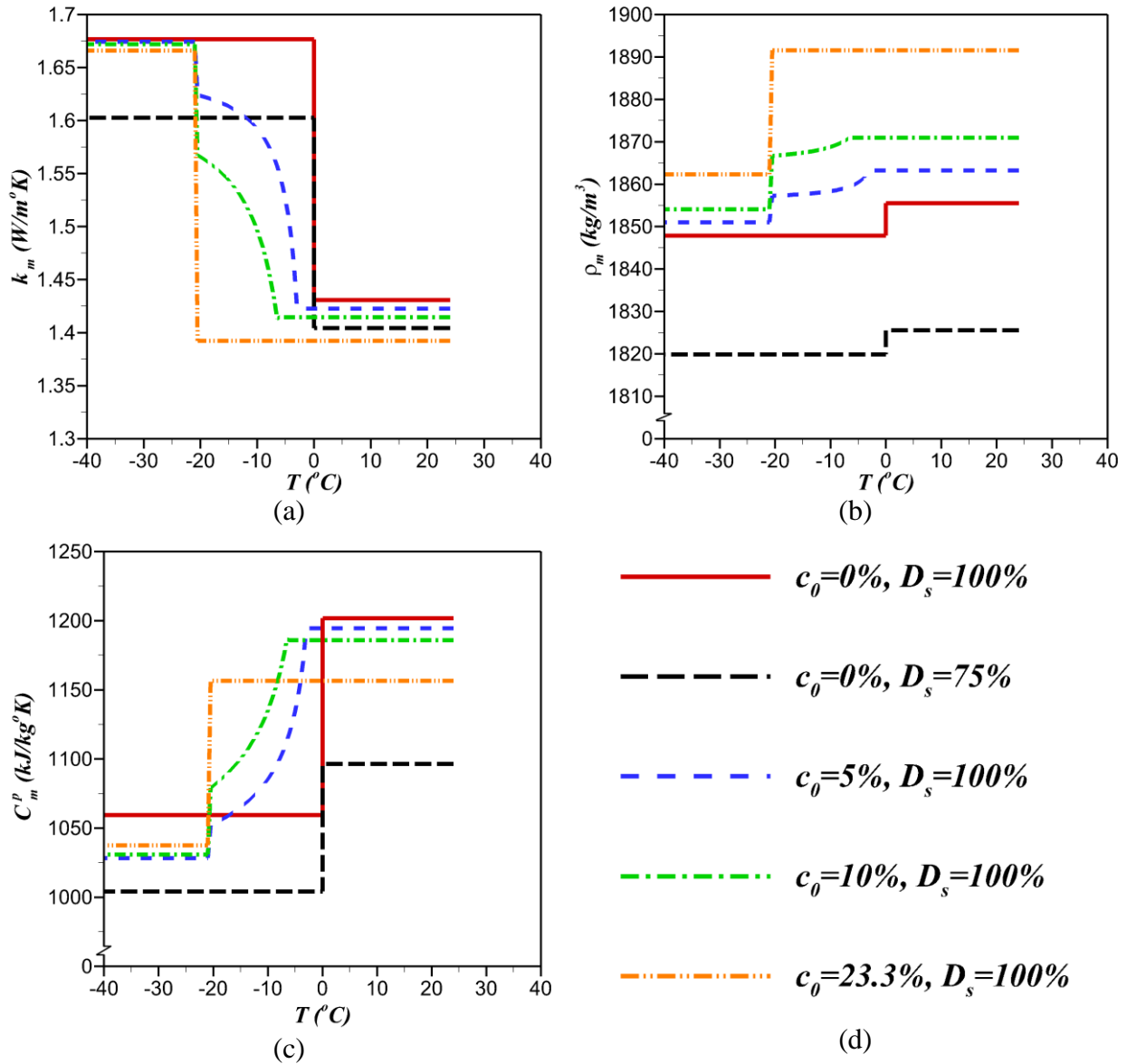299 the mortar pores (i.e., air, ice, and solution).

300 The law of mixtures was again employed to obtain the effective density of the materials in the

301 mortar's pores (i.e., ρ_P) as described in Equation 11.

$$\rho_P = \rho_{air} \cdot v_{air} + v_F \cdot \left[\rho_{ice} \cdot \xi + \left(1 - \xi\right) \cdot \rho_{so\ln}\right] + \rho_{so\ln} \cdot v_w$$

11

302 where ρ_{air}, ρ_{ice}, and $\rho_{so\ln}$ are the densities of air, ice, and solution, respectively. The

303 corresponding densities of air, ice, NaCl solution with different concentrations, and dry mortar

304 are also provided in Table 1.

Table 1 Thermal properties of air, ice and NaCl solution with different concentrations

Material	k (W/(m·K))	ρ (kg/m³)	C^p (kJ/(kg·K))
Air [63, 64]	0.023	1.35	1.005
Ice [65]	2.25	934	2030
0% NaCl solution [66]	0.5886	997	4121
5% NaCl solution [66]	0.5611	1036	3947
10% NaCl solution [66]	0.5336	1074	3773
23.3% NaCl solution [66]	0.46	1178	3310
Dry mortar [67–69]	1.7	2070	850

Figure 5 Calculated effective (a) thermal conductivity $\left(k_m\right)$; (b) density $\left(\rho_m\right)$; and (c) specific heat capacity $\left(C_m^p\right)$ as a function of temperature for mortar specimens containing (d) various concentrations of NaCl solutions and different degrees of saturation.

305   *5.3. Specific heat capacity, C^p*

306   The process of determining an effective specific heat capacity is conceptually similar to

307   determining an effective density [70]. The effective specific heat capacity for a composite mortar

308   specimen C_m^p was calculated using Equation 12 and is shown in Figure 5c.

$$C_m{}^p \cdot \rho_m = C_{dry}{}^p \cdot \rho_{dry} \cdot (1 - v_P) + C_P{}^p \cdot \rho_P \cdot (v_P) \qquad \textbf{12}$$

309   where C_{dry}^p is the specific heat capacity of the dry mortar and C_P^p is the effective specific

310   heat capacity of materials in the mortar pores (i.e., air, ice and solution) which can be calculated

311   using Equation 13.

$$C_P^p \cdot \rho_P = C_{air}^p \cdot \rho_{air} \cdot v_{air} + \left\{ \begin{array}{l} v_F \cdot \left[C_{ice}^p \cdot \rho_{ice} \cdot \xi + C_{so\ln}^p \cdot \rho_{so\ln} \cdot (1 - \xi) \right] \\ + C_{so\ln}^p \cdot \rho_{so\ln} \cdot (v_w) \end{array} \right\} \qquad \textbf{13}$$

312   where C_{air}^p, C_{ice}^p, and $C_{so\ln}^p$ are the specific heat capacities for air, ice, and solution,

313   respectively. The corresponding specific heat capacities of air, ice, NaCl solution with different

314   concentrations, and dry mortar are provided in Table 1.

315

316 **6. Configuration of numerical simulation and boundary conditions**
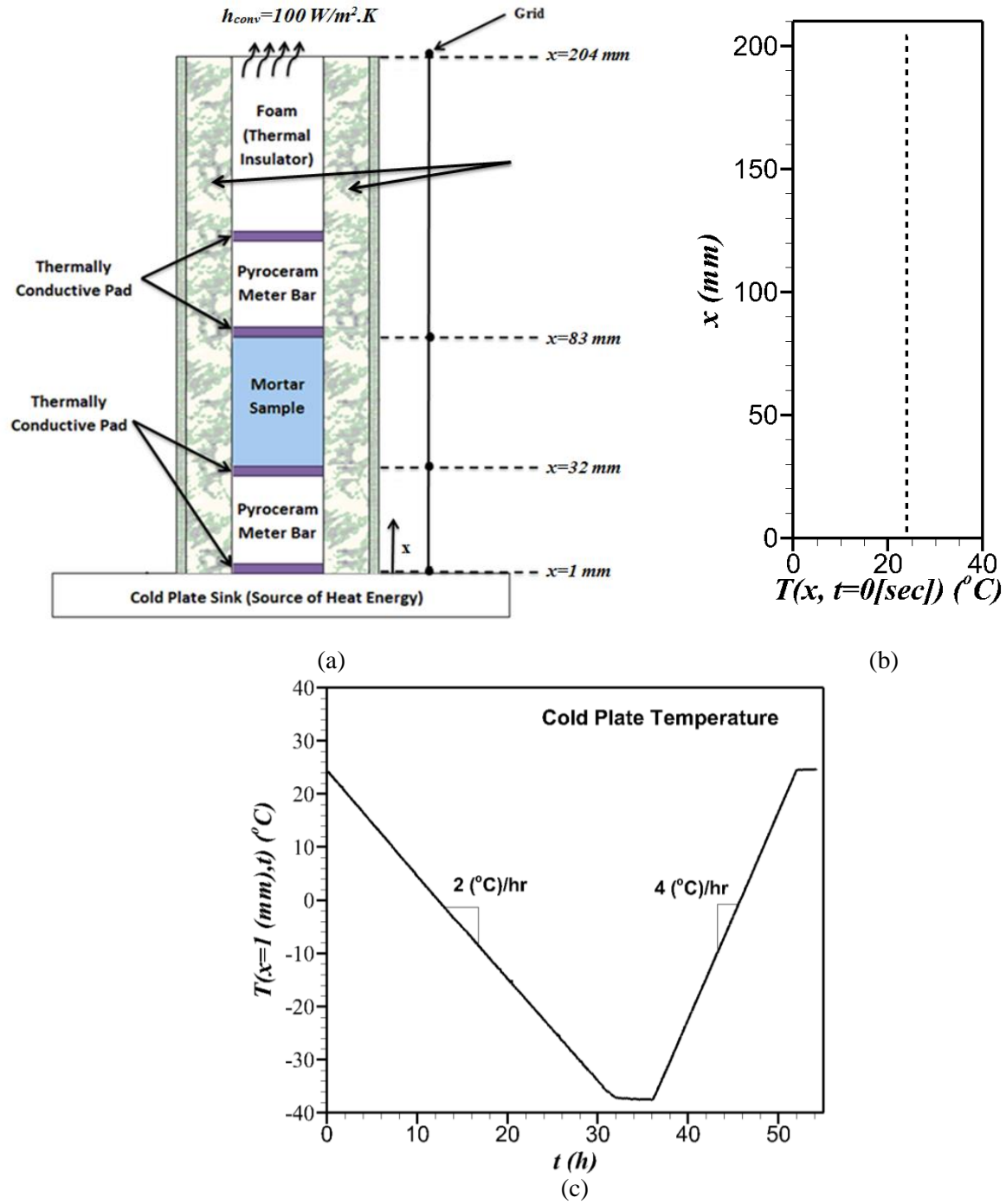
317   Following the work by Farnam et al. [9], the LGCC test was simulated to quantify heat flow

318 and predict the temperature profiles of the mortar specimens. Two types of experimental data are

319 used: 1) fully saturated mortar specimens (i.e., 100 % degree of saturation) with solutions

320 containing 0 %, 5 %, 10 %, and 23.3 % NaCl (by mass), and 2) specimens saturated partially

321 with water (i.e., no NaCl involved in the solution) at degrees of saturation equal to 75 %, 85 %,

322 95 %, and 100 %. The procedures used for preparation of fully saturated and partially saturated

323 mortar specimens were addressed in previous experimental works [9, 12, 71].

324   The experimental conditions of one-dimensional heat transfer were provided in the LGCC

325 experiment by using a heat sink at the bottom, longitudinal insulation on the sides, and foam as a

326 thermal insulation around the system to minimize the heat dissipation from the experimental

327 apparatus (Figure 6a). However, a difference between the measured released heat in an LGCC

328 experiment and the associated enthalpy of fusion of phase change materials (i.e., Methyl Laurate

329 and Paraffin Oil), likely due to experimental imperfections (thermal bridges, heat leaks, etc.),

330 was observed. Therefore, h_{loss}, a heat loss coefficient, is employed to simulate the energy

331 dissipation in the experimental system which is estimated as a 40 % to 60 % heat loss [72]. It is

332 worth mentioning that the advection of heat to simulate the water transport occurring during the

333 freeze/thaw cycle is neglected in this numerical investigation.

334   Two reference (meter) bars made of Pyroceram code 9606[†] with known thermal properties

335 were used to measure the heat flow passing through the mortar specimen in the experiment (see

336 Figure 6a.

[†] Certain commercial products are identified in this paper to specify the materials used and procedures employed. In no case does such identification imply endorsement or recommendation by the National Institute of Standards and Technology or Purdue University, nor does it indicate that the products are necessarily the best available for the purpose.

Figure 6 (a) Schematic view of LGCC experiment with adapted finite difference nodes; (b) initial temperature of finite difference simulation, i.e., $T(x, t = 0)$; and (c) temperature at the bottom of the LGCC experiment, i.e., $T(x = 1, t)$, as a function of time.

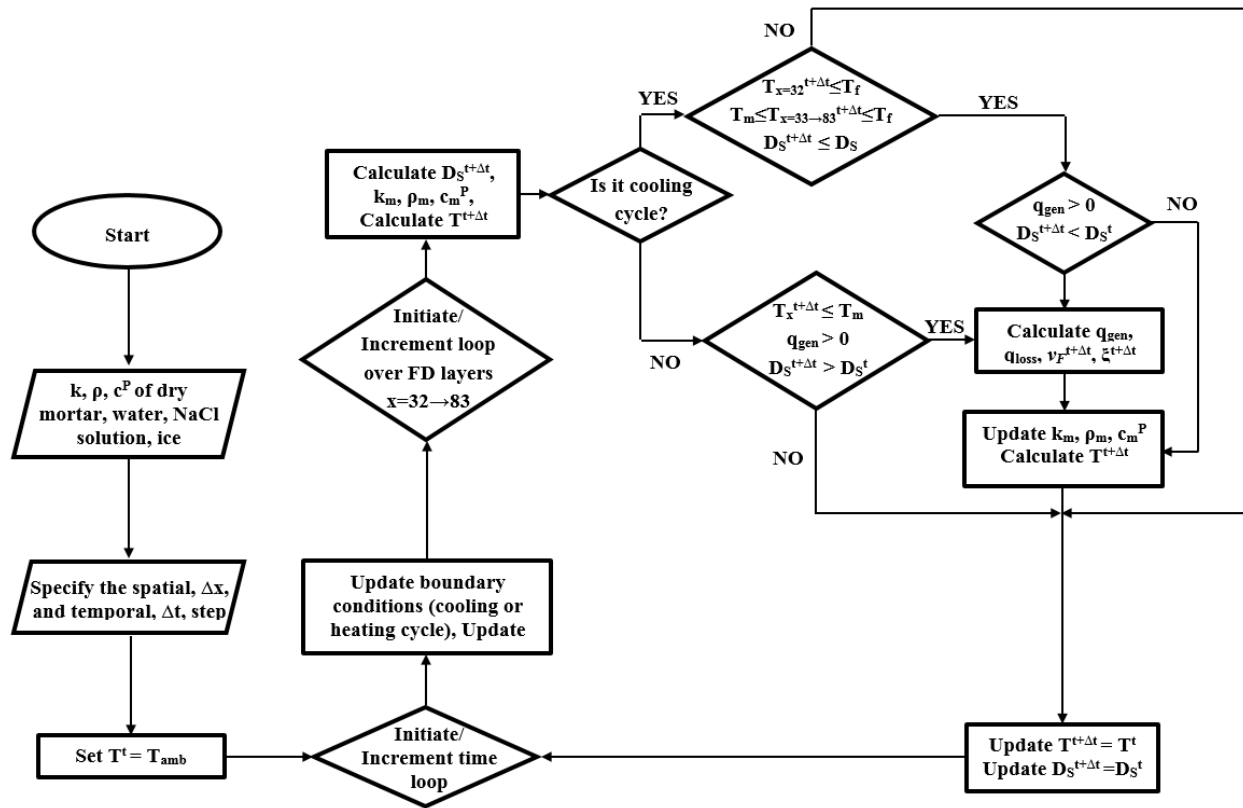**Table 2** Thermal properties of thermally conductive pad, foam and Pyroceram code 9606

Material	k (W/(m·K))	ρ (kg/m^3)	C^p (kJ/(kg·K))
Thermal Pad	3.0	309	850
Foam [73]	0.03	20	1340
Pyroceram Code 9606 [9]	*	2600	900

Note: *The thermal conductivity of Pyroceram code 9606 as a meter bar material was calculated as a function of temperature [9].

337   The first step in the numerical approach was to discretize the experimental setup by a finite

338   difference method using an appropriate grid spacing size, Δx of 1 (mm) and time step, Δt of

339   0.05 (sec). The initial temperature of the entire experimental setup was set equal to the ambient

340   temperature $T(x, t=0) = 24$ (°C) as displayed in Figure 6b. The temperature at the bottom of the

341   LGCC experiment, $T(x = 1\ mm, t)$ (see Figure 6a) varied in the numerical simulation as a

342   function of time according to the LGCC experimental protocol (Figure 6c). A heat convection

343   coefficient $h_{conv} = 100$ W/(m^2·K) is employed to simulate the heat transfer between the air and

344   the foam on the top [54]. Even though the insulating foam has a quite small thermal diffusivity

345   parameter, significant heat energy is still transferred to the environment, resulting in a slight

346   temperature differential between the top of the foam and the ambient environment. The relevant

347   thermal properties of the thermally conductive pad, foam, and Pyroceram code 9606 used in the

348   modeling are listed in Table 2.

349   Figure 7 displays a flow chart of the one-dimensional explicit finite difference method

350   adopted to simulate the saturated mortar specimen containing de-ionized water and NaCl

351   solution with various concentrations. First, the thermal properties of components of the mortar

352   specimen, temporal and spatial step sizes, and thermal initial and boundary conditions are

353   determined. All of the discretized layers (i.e. x = 1 mm to x = 204 mm) are employed to simulate

354   the heat transfer for the LGCC experiment; however, only the finite layers of the mortar

355   specimen (i.e., x = 32 mm to x = 83 mm) are investigated in this figure. During phase

356   transformation of the pore solution in the mortar specimen filled with de-ionized water, two

357   approaches of consideration of either a discrete pore size distribution or a continuous pore size

358   distribution were employed, as discussed in section 3. The approach of using a distribution of

359   continuous pore sizes introduces a progressive ice formation/melting in the pores that is

360   simulated using equations 3 and 4 and figure 1; however, the volume fraction of pores with the

361   size greater than $5\,nm$ ($v_F = 60\,\%$) is considered to simulate the instantaneous ice

362   formation/melting occuring in the approach of using discrete pore sizes. Additionally, the

363   progressive fraction of produced/melting ice is calculated using the lever rule as discussed in

364   section 4.

Figure 7 Numerical algorithm of finite difference strategy using heat transfer equation to simulate the thermal behavior of a saturated mortar specimen.

365 **7. Undercooling**

366   The freezing temperature T_f is the point at which solidification of a liquid occurs, whereas a

367   melting temperature T_m is the point at which a solid melts. In most materials, T_f is usually lower

368   than T_m because of undercooling [28–30]. Therefore, no ice may be formed until the temperature

369   reaches T_f (see Figure 4a). The values of T_f and T_m are obtained directly from the LGCC

370   experiment [9] and are reported in Table 3.

Table 3 Freezing and melting points of saturated mortar specimens with NaCl solutions [11]

NaCl Solution Concentration (%)	Freezing Point T_f (°C)	Melting Point T_m (°C)	Amount of Undercooling with Respect to Liquidus Line**
0	-6.1	0.0	-6.1
5	-10.8	-3.0	-7.8
10	-12.0	-6.5	-5.5
23.3*	-21.1	-21.1	0

371   Note: *For specimens containing 23.3% NaCl solution, the freezing point and melting point are identical (T_{eut}) since these points
372   are located at the eutectic line and the entire solution only forms eutectic solid during solidification.
373   ** The amount of undercooling is calculated by subtracting the melting point T_m from the freezing point T_f of the
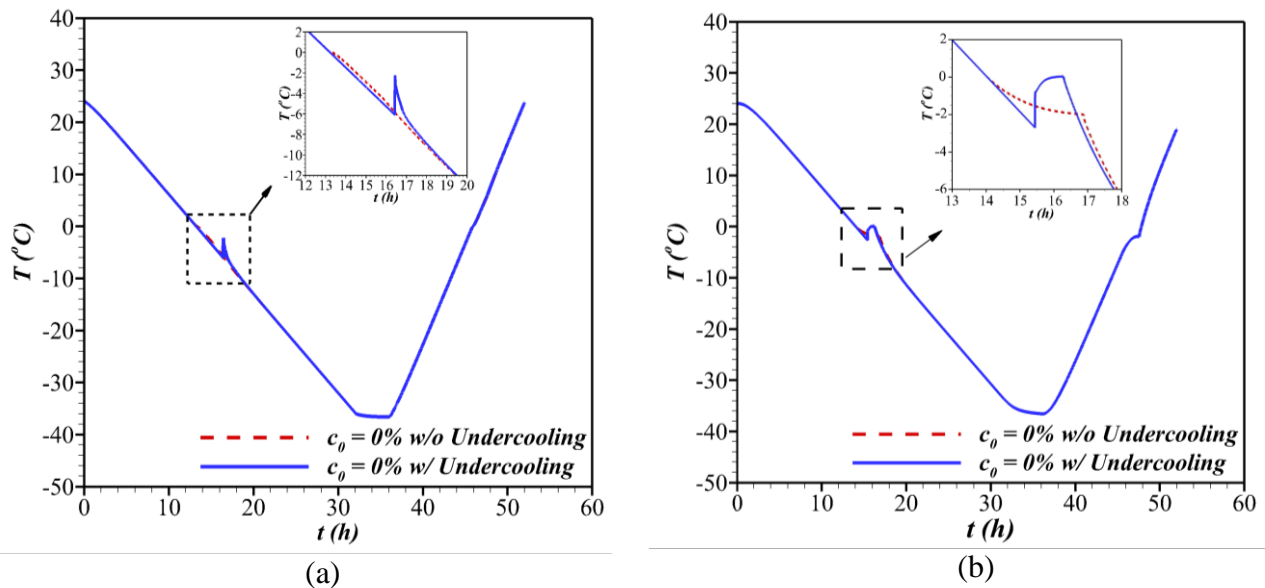374   corresponding bulk NaCl solution.

375   The specimen size and cooling rate of the specimen may alter the degree of undercooling

376   [27]. In general, less undercooling is observed for larger specimens (greater chance of a suitable

377   nucleation source being present), while more undercooling is observed when a greater cooling

378   rate is employed. In the LGCC test (a 25 mm x 25 mm x 50 mm mortar specimen size), the

379   freezing was observed at -6.1 °C when the mortar was saturated with water.

380   When the temperature of the bottom layer reaches T_f, the layers with temperatures lower than

381   T_m are allowed to begin to produce ice instantaneously and thus the associated heat release

382   results in increasing the temperature toward T_m. Subsequently, the temperature of the layer

383   remains unchanged at T_m until the entire liquid within that layer transforms into ice. Since the

384   numerical model with a discrete pore size distribution is considered to investigate the

385   undercooling effect on thermal behavior of the mortar specimen, nearly 60 % of the pores by

386   volume (i.e., nearly all of the capillary pores, air-entrained pores, and air-entrapped pores)

387   nucleate ice instantaneously for the case of the mortar specimen saturated with deionized water

388   (solution with 0 % NaCl concentration), as shown in Figure 8.

389   Figure 8 illustrates the effect of considering undercooling on the thermal behavior of the

390   simulated mortar specimens saturated with de-ionized water solution compared with the model

391   without undercooling. The heat loss coefficient, h_{loss} is assumed to be a constant value of 60 % in

392   this figure. Similar to the observed experimental thermal behavior of the mortar specimen [9], a

393   temperature rise at the freezing point was observed in the phenomenological numerical model

394   when undercooling was included, whereas no abrupt temperature ascent was observed without

395   including undercooling. It is worth mentioning that no considerable changes in the dimensions of

396   the mortar specimens were measured during the freezing and melting processes in the

397   experiment.

(a)   (b)

Figure 8 The effect of including undercooling in the numerical simulation on temperature profile of saturated mortar specimen containing water (0 % NaCl) exposed to one freeze-thaw cycle at different locations of mortar specimen: (a) x = 32 mm; (b) at x = 83 mm (see Figure 1 for definition).

398   **8. Results**

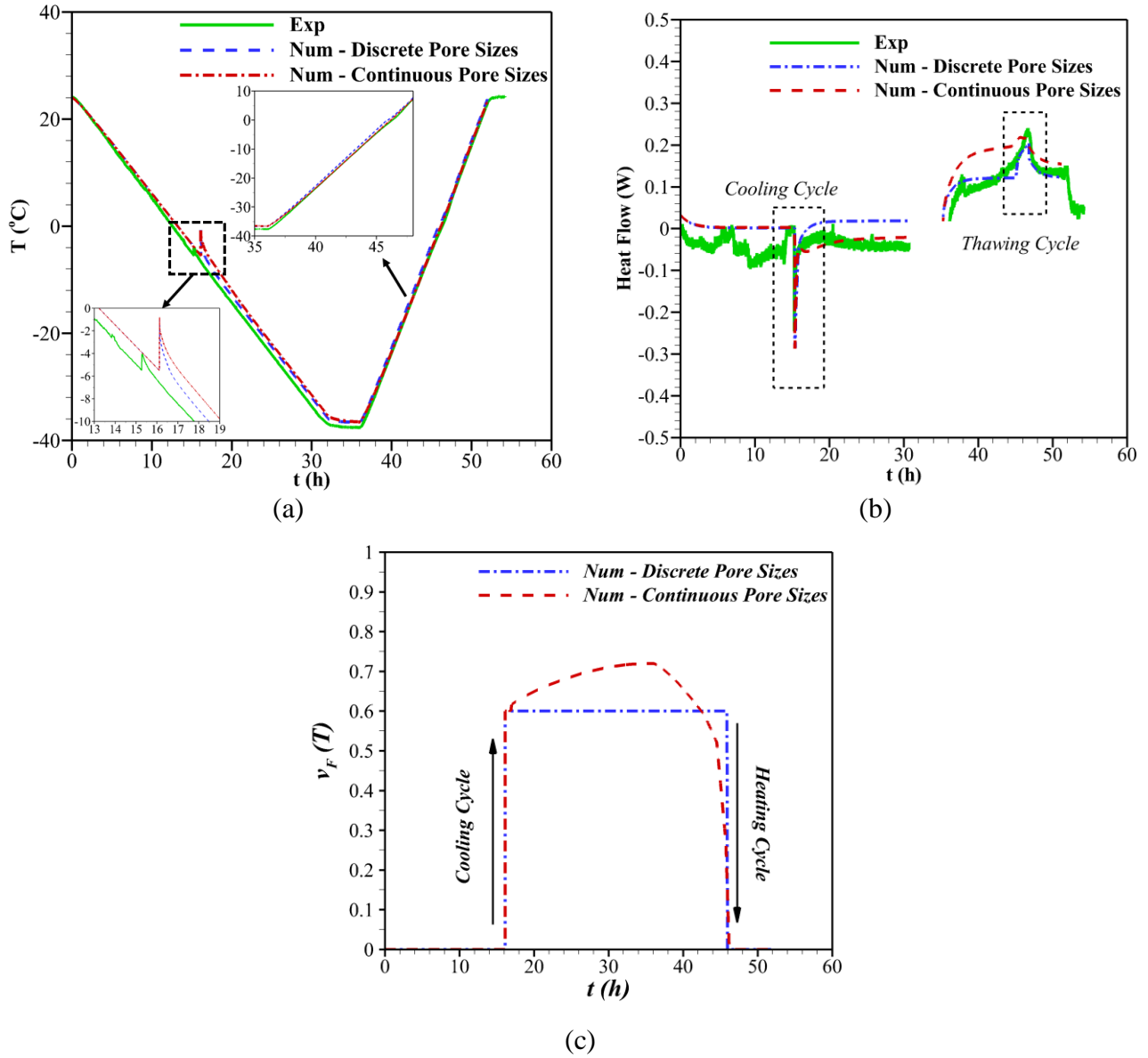399   *8.1. Mortar specimens saturated with water*

400   In this section, mortar specimens saturated with water at 75 %, 85 %, 95 % and 100 %

401   degrees of saturation (D_S) and the effect of pore size distribution are numerically investigated.

402   *8.1.1. Fully saturated mortar specimen*

403   Two numerical models, with either a continuous or discrete pore size distribution, are

404   investigated in this section. Figure 9 shows the experimental and numerical results for the

405   thermal behavior of mortar specimens that were saturated (i.e., $D_S = 100$ %) with water. The heat

406   loss coefficient, h_{loss} is assumed to be a constant value of 60 % in this figure. The model with a

407   discrete pore size distribution only considers the instantaneous freezing of the pore solution that

408   can freeze ($v_F = 60\%$), whereas the model with the continuous pore size distribution also

409   considers an additional process of gradual freezing of the pore solution ($v_F = 72\%$) as displayed

410   in Figure 9c. Figure 9a indicates the numerical and experimental temperature profile for the

411   saturated mortar specimen at the bottom layer in the LGCC experiment setup (i.e., $x = 32$ mm). A

412   nearly instantaneous temperature rise that occurred at the moment of freezing can be observed,

413   demonstrating the instantaneous freezing due to the temperature of the first finite difference layer

414   of the mortar specimen (i.e., $x = 32$ mm) reaching the freezing temperature of (undercooled)

415   water in the mortar specimen ($T_f = -6.1$ °C). However, the model with a continuous pore size

416   distribution considers that the remaining amount of unfrozen water in the pores transforms to ice

417   gradually until the temperature reaches -35 °C.

418   The model with a discrete pore size distribution considers the ice melting to occur by

419   absorbing sufficient heat at the melting temperature of the large frozen pores observed in the

420   experiment ($T_m = 0$ °C). In the model with a continuous pore size distribution included, the ice

421   formed in the pores is considered to melt gradually starting at $-35\,^{\circ}\text{C}$ [24], based on the

422   measured absorption isotherm for the mortar.

(a)

(b)

(c)

Figure 9 Experimental and numerical results for mortar specimen fully saturated with water (a) temperature profiles at $x = 32$ mm (see Figure 1 for definition of x); (b) predicted heat flow; (c) volume of pore solution undergoes phase transformation at the bottom surface of the mortar specimen.

423   The heat flow is obtained using the numerical simulation to evaluate the role of pore size

424   distribution and compared to the experimental data shown in Figure 9b. The formation of ice in

425 the pore solution results in an exothermic peak, which is representative of the latent heat release

426 during a freezing cycle. In the model with a discrete pore size distribution, the exothermic peak

427 is considered to occur at T_f and subsequently ceases when the entire amount of latent heat has

428 been emitted to the surroundings. The endothermic peak begins as a gradual process at $0\,°C$, until
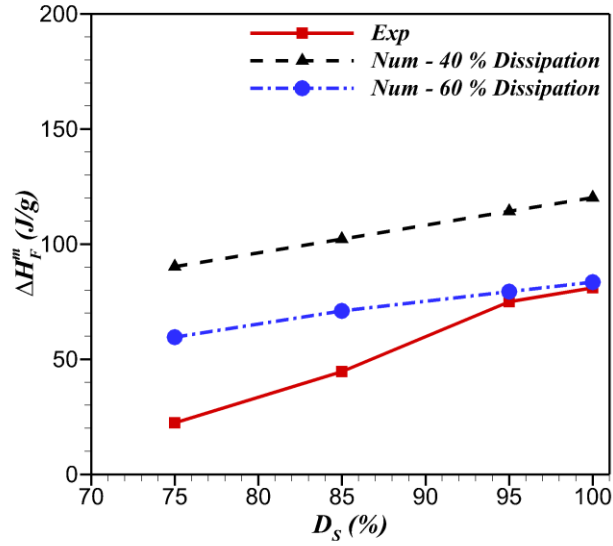
429 all of the previously formed ice melts inside the frozen pores.

430 Conversely, the exothermic peak is extended to the end of the freezing cycle ($-35\ °C$) due to

431 gradual ice nucleation inside the smaller pores in the model with a continuous pore size

432 distribution. For the case of melting, the endothermic peak is considered to occur gradually as a

433 function of temperature and the pore size.

434 Therefore, the melting curve extends progressively to $0\,°C$, owing to the broad range of pore

435 sizes in the model with a continuous pore size distribution. It is concluded that the consideration

436 of pore size distribution can reasonably be neglected during the freezing process due to

437 undercooling, whereas the melting of formed ice indicated a gradual process as the temperature

438 increases in both the experimental data and the model with a continuous pore size distribution.

439 *8.1.2. Partially saturated mortar specimen*

440 The amount of heat released during freezing $\left(\Delta H_m^F\right)$ was obtained using the numerical

441 simulation for mortar specimens saturated at different degrees of saturation with the discrete pore

442 size distribution model and is compared with experimental results in Figure 10. For partially

443 saturated samples, the value of v_F was calculated using $v_F = D_S\text{-}v_w$, where v_w is the volume fraction

444 of pores with the size less than 5 nm ($v_w = 40\ \%$). The results for these partially saturated mortar

445 specimens are the experimental investigation of this work, whereas the experimental data of the

446 fully saturated mortar specimen was already published [9]. Two heat dissipation coefficients of

447   40 % and 60 % are considered as discussed in section 6. The coefficient of variation for the

448   experimental results is obtained as 8.6 %. The numerical simulation predicts greater heat release

449   than that obtained in the experiment due to further experimental imperfections.

Figure 10 The amount of heat release during freezing $\left(\Delta H_m^F\right)$ for the mortar specimen saturated at different degrees of saturations $\left(D_S\right)$.

450   *8.2. Mortar specimens saturated with NaCl solution*

451   The role of NaCl concentration in the pore solution on the thermal behavior of the mortar

452   specimens was also investigated. The process of solidification of the brine solution absorbed in

453   the large pores with a high degree of connectivity is investigated in this model. Therefore, the

454   volume fraction of freezable pore solution containing NaCl solution is assumed to be 60 %.

455   Afterwards, the parameter $\xi(T)$ is employed to calculate the volume fraction of frozen pore

456   solution $v_F(T)*\xi(T)=0.6*\xi(T)$ using the Lever rule (based on the phase diagram of NaCl

457   solution). Since it is proposed that the pores larger than gel pores are susceptible to freezing in

458   this numerical model, the size of a salt crystal is sufficiently large so as not to increase its

459   solubility correspondingly. As mentioned in section 7, undercooling compels the solutions inside
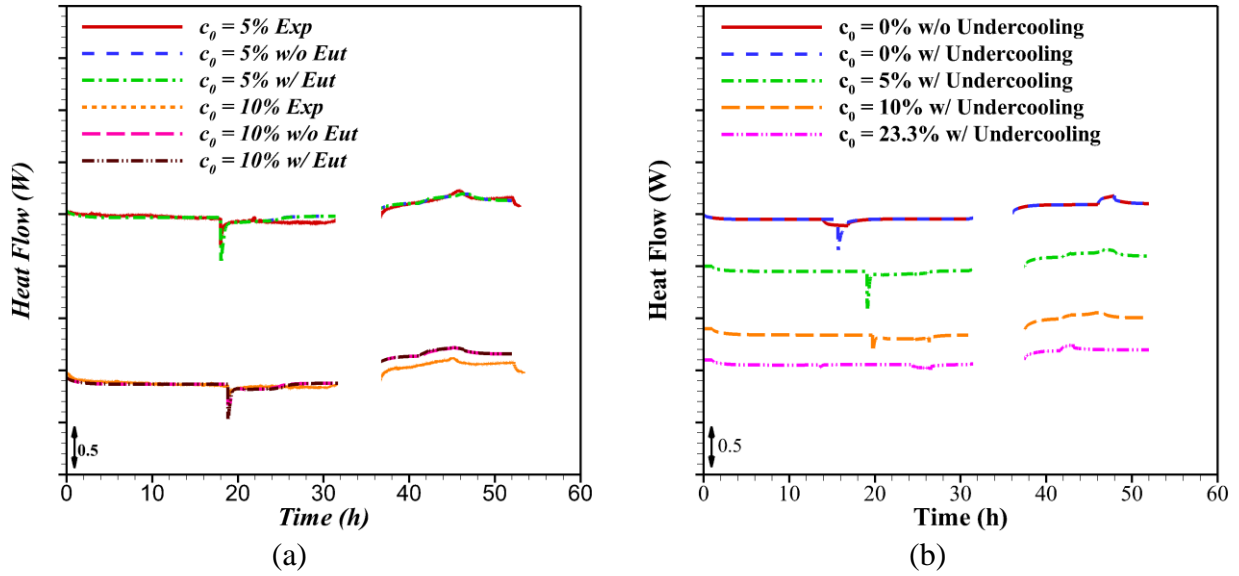
460   the porous media to freeze at a temperature below their melting points which can result in an

461   instantaneous solidification of a relatively large fraction of pore solution within the mortar

462   specimen (see Table 3). After this sudden freezing, a gradual phase transformation of the water

463   phase of the solution to ice is hypothesized to occur for the remaining solution in the mortar

464   specimen saturated with NaCl solution. This was computed by using the lever rule approach to

465   solidify the remaining unfrozen fraction of solution (excluding the eutectic solution) until the

466   temperature of each layer reaches $T_{eut} = -21.1\,°C$. For the case of mortar specimens saturated

467   with 23.3 % NaCl solution ($c_{eut} = 23.3\%$), no ice is formed until the temperature decreases to

468   T_{eut}.

469   At this temperature, the unfrozen eutectic solution begins to transform to eutectic ice

470   gradually. Two different procedures are proposed to investigate the role of eutectic solution

471   solidification on the macro-scale thermal response of the mortar specimen. The first method

472   considers that the eutectic solution, the remaining unfrozen solution, can gradually form eutectic

473   ice by releasing the eutectic latent heat as observed in the experiment shown in Figure 11a [9].

474   The second method was to allow the eutectic solution to migrate to the adjacent accessible pores

475   with smaller sizes to avoid the formation of eutectic ice in the numerical simulation. Finally, the

476   numerical results were compared with macro-scale experimental data. The numerical and

477   experimental results of heat flow of two mortar specimens saturated by NaCl solutions with 5 %

478   and 10 % concentrations are compared in Figure 11a. The variation of the two numerical models

479   is calculated as 3 % which indicates that the eutectic phase transformation of the NaCl solution

480   should be considered in the numerical modeling. Figure 11b shows the heat flow as a function of

481   time obtained from the numerical simulation for the specimen saturated with NaCl solution while

482   this figure compares the thermal behavior of a mortar specimen with and without undercooling.
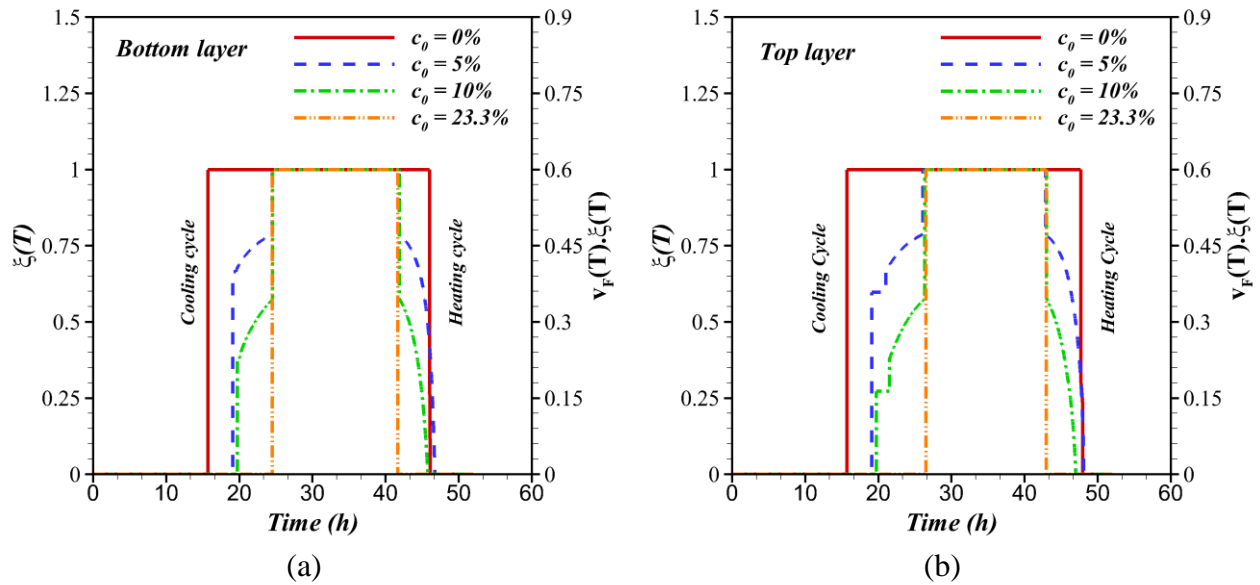
483   First, a broader exothermic peak in the heat flow is observed for the numerical simulation

484   without undercooling, since a more gradual freezing is considered. Second, the ice formation

485   occurs earlier in the case of the mortar specimen without including undercooling, since the

486   freezing point T_f is assumed to be identical to the melting temperature T_m. Third, the

487   exothermic peak becomes smaller by increasing the NaCl solution concentration, since a lower

488   volume fraction of pore solution freezes at the corresponding freezing point T_f, which results in

489   a lower heat release through the mortar specimen. Fourth, the exothermic peak of the mortar

490   specimens saturated with greater NaCl solution concentrations occurs later due to depression of

491   the freezing point T_f. The heat loss coefficient, h_{loss} is assumed to be a constant value of 60 % in

492   this figure. Figure 12 displays how pore solution solidifies/melts during cooling/heating at the

493   bottom and top layers (surfaces) of the mortar specimen since the temperature difference is the

494   maximum between these layers. At the bottom layer, solution containing NaCl first freezes

495   suddenly when reaching T_f due to undercooling effects. Afterwards, ice gradually forms as the

496   temperature further decreases until the temperature reaches T_{eut} at the bottom layer of the mortar

497   specimen. At T_{eut}, all liquid solidifies in the capillary, entrained air, and entrapped air pores.

498   As described in section 7, at the moment of sudden freezing (when the temperature of the

499   bottom layer reaches T_f), the portion of the mortar specimen whose temperature is between T_f

500   and T_m was allowed to freeze instantaneously. Since the temperature of the top layer of the

501   mortar specimen is higher than the temperature at its bottom layer during a cooling cycle, a

502   lesser amount of ice is produced at the top layer during the sudden freezing (i.e., undercooling)

503   in comparison to the bottom layer, as can be seen in Figure 12. The remainder of the pore

504   solution begins to freeze as the temperature of the layer drops. This solidification process is

505   similar between the bottom and top layers of the mortar specimen containing 0 % NaCl solution,

506   since this process takes place immediately (0.04 seconds). During heating, the melting

507   transformation occurs gradually and the amount of ice can be simply calculated based on the

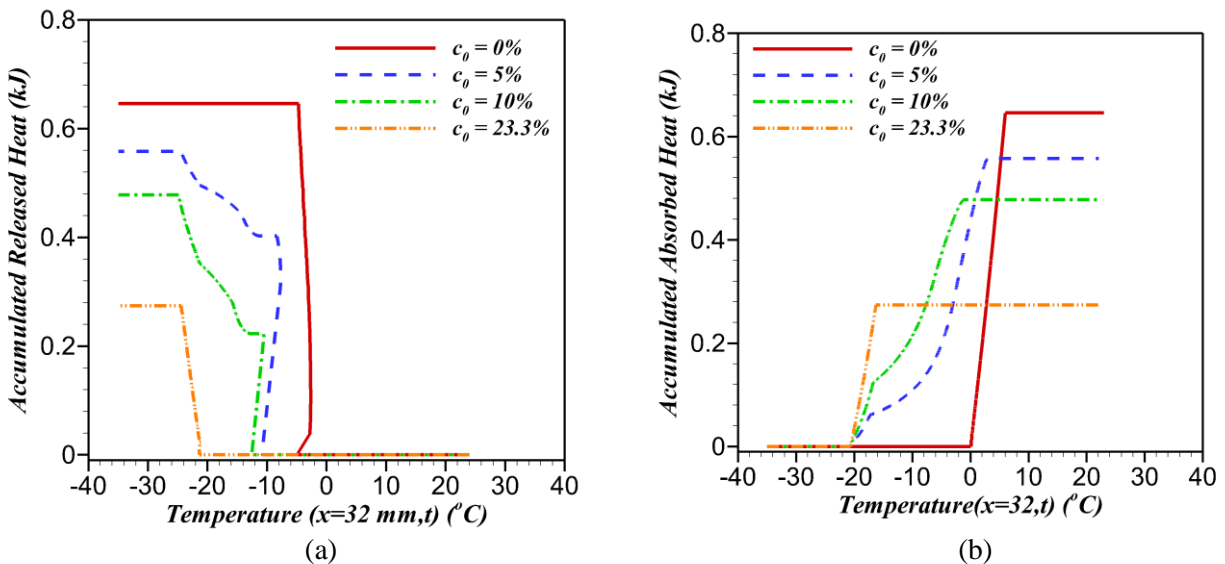508   lever rule, since no undercooling occurs.

(a)   (b)

Figure 11 Heat flow as a function of time for mortar specimens saturated with NaCl solution obtained from (a) experimental results and numerical simulation to investigate the role of eutectic phase transformation; (b) numerical simulations at various concentrations (0 %, 5 %, 10 %, 23.3 %).

(a)   (b)

Figure 12 Frozen fraction of pore solution of the mortar specimen saturated using NaCl solution as a function of time at (a) the bottom layer (x = 32 mm); and (b) the top layer (x = 83 mm).
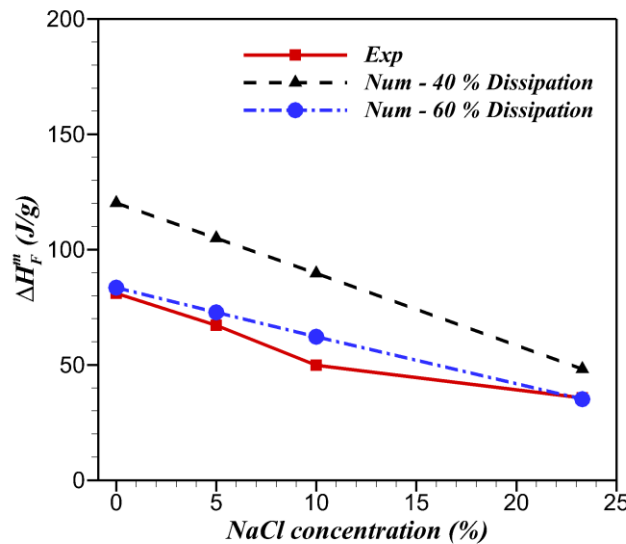
509   It is worth mentioning that there is therefore relatively no difference in the melting behavior

510   of pore solution between the top and the bottom layers of the mortar specimen. Figure 13 shows

511   the accumulated released/absorbed heat by the mortar specimen as a function of its bottom layer

512   temperature (i.e., ($x = 32$ mm)). Pore solutions containing 0 %, 5 %, and 10 % NaCl illustrate a

513   relatively extreme heat emission due to freezing, while the solution containing 23.3 % NaCl

514   releases relatively little energy as it is only composed of the eutectic composition (see Figure

515   13a). A snapback (rise) of temperature is observed at freezing onset due to the undercooling of

516   pore solution. Figure 13b displays how the specimen absorbs heat during heating/melting. Since

517   melting is a gradual process, the heat absorption occurs at a relatively gradual rate with respect to

518   the freezing process. It is worth mentioning that the total amount of released heat during freezing

519   is identical to the total amount of absorbed heat during melting in the system. The heat loss

520   coefficient, h_{loss} is assumed to be a constant value of 60 % in this figure.

(a)   (b)

Figure 13 Accumulated heat as a function of temperature for mortar specimen with 5 %, 10 %, and 23.3 % NaCl concentration (a) heat released by the specimen during one freezing cycle; (b) heat absorbed by the specimen during one thawing cycle versus cold plate temperature.

521   The amount of heat released during freezing $\left(\Delta H_m^F\right)$ is numerically obtained and plotted as a

522   function of NaCl concentration and compared with experimental results in Figure 14. It is worth

523   mentioning that the coefficient of variation for the experimental results is obtained as 8.6 %,

524   based on three replicate specimens. The numerical results are calculated by considering the two

525   coefficients of heat dissipation h_{loss} to compare to the experimental data. Considering these heat

526   dissipation coefficients, the coefficient of variation between experimental result and numerical

527   results with 40 % and 60 % are obtained as 36 % and 9 %, respectively. The numerical over-

528   prediction of latent heat emission is caused by further experimental imperfections.

Figure 14 The amount of heat release during freezing $\left(\Delta H_m^F\right)$ for the mortar specimen saturated with different NaCl solutions.

529   **9. Summary and Conclusion**

530   In this paper, a one-dimensional finite difference numerical model was used to predict the

531   macroscopic freeze-thaw behavior of air-entrained mortar specimens. The effective thermal

532   properties of the composite mortar were estimated using homogenization techniques. The role of

533   curvature, owing to a broad range of pore sizes, was considered in calculating the volume

534 fraction of freezable pore solution exposed to freezing/thawing cycles using measured

535 absorption-desorption isotherms. It was concluded that the role of pore size (or curvature) on the

536 macroscopic behavior of the air entrained mortar specimen was negligible during freezing due to

537 the quantity of larger pore sizes in realistic mixtures and undercooling, whereas the role of

538 curvature had a considerable impact on the macroscopic behavior of the frozen mortar specimen

539 during melting. The lever rule approach, derived from a phase diagram of the NaCl-water

540 solution, and undercooling were adopted in the numerical model. It was concluded that this

541 model can simulate the freezing and thawing process of mortar specimens saturated with water

542 or various NaCl solutions to predict the thermal behavior of mortar specimens at various degrees

543 of saturation or saturated with various concentrations of NaCl solutions.

544 The computational results were compared to the experimental ones obtained for mortar

545 specimens saturated with NaCl solution using a low-temperature longitudinal guarded

546 comparative calorimeter (LGCC). A lower amount of heat release (or freezable fraction of pore

547 solutions) was observed in the experiment than the theoretical value predicted based on the

548 measured desorption isotherm. The difference may be mainly due to experimental conditions

549 allowing significant heat dissipation within the LGCC experiment. To justify the experimental

550 under-estimation of heat release, two heat loss coefficients of 40 % and 60 % were evaluated to

551 validate the numerical results. Accordingly, a better agreement was exhibited between the

552 numerical results and the experimental data.

References

1. Powers T C, and Willis T F (1950) The air requirement of frost resistant concrete. Highw Res Board 29:184–211.

2. Powers TC (1945) A working hypothesis for further studies of frost resistance of concrete. Am Concr Cem Portl Cem Assoc 41:245–272.

3. Powers TC (1900) The physical structure and engineering properties of concrete.

4. Litvan G (1976) Frost action in cement in the presence of De-Icers. Cem Concr Res 6:351–356.

5. Scherer G (1999) Crystallization in pores. Cem Concr Res 29:1347–1358.

6. Kaufmann J (2000) Experimental identification of damage mechanisms in cementitious porous materials on phase transition of pore solution under deicing salt attack. École polytechnique fédérale de Lausanne (EPFL)

7. Mehta, P. K. and Monteiro PJ (2006) Concrete: Microstructure, Properties, and Materials. McGraw-Hill, New York

8. Spragg RP, Castro J, Li W, et al. (2011) Wetting and drying of concrete using aqueous solutions containing deicing salts. Cem Concr Compos 33:535–542.

9. Farnam Y, Bentz D, Sakulich A, et al. (2014) Measuring freeze and thaw damage in mortars containing deicing salt using a low-temperature longitudinal guarded comparative calorimeter and acoustic emission. Adv Civ Eng Mater 3:20130095.

10. Villani C, Farnam Y, Washington T, et al. (2015) Performance of conventional portland cement and calcium silicate based carbonated cementitious dystems furing freezing and thawing in the presence of calcium chloride deicing salts. Transp. Res. Board.

11. Farnam Y, Bentz D, Hampton A, Weiss W (2014) Acoustic emission and low-temperature calorimetry study of freeze and thaw behavior in cementitious materials exposed to sodium chloride salt. Transp Res Rec J Transp Res Board 2441:81–90.

12. Farnam Y, Todak H, Spragg R, Weiss J (2015) Electrical response of mortar with different degrees of saturation and deicing salt solutions during freezing and thawing. Cem Concr Compos 59:49–59.

13. Farnam Y, Wiese A, Bentz D, et al. (2015) Damage Development in Cementitious Materials Exposed to Magnesium Chloride Deicing Salt. Constr Build Mater 93:384–392.

591   14. Han B, Choi JH, Dantzig J a, Bischof JC (2006) A quantitative analysis on latent heat of an
592   aqueous binary mixture. Cryobiology 52:146–51.

593   15. Radjy F (1968) A thermodynamic study of the system hardened cement paste and water and
594   its dynamic mechanical response as a function of temperature.

595   16. Young JF (1988) A review of the pore structure of cement paste and concrete and its
596   influence on permeability. 108:1–18.

597   17. Whiting DA, Nagi MA (1998) Manual on control of air content in concrete.

598   18. Kumar R, Bhattacharjee B (2003) Porosity, pore size distribution and in situ strength of
599   concrete. Cem Concr Res 33:155–164.

600   19. Castro J, Bentz D, Weiss J (2011) Effect of sample conditioning on the water absorption of
601   concrete. Cem Concr Compos 33:805–813.

602   20. Sun Z, Scherer GW (2010) Effect of air voids on salt scaling and internal freezing. Cem
603   Concr Res 40:260–270.

604   21. Li W, Pour-Ghaz M, Castro J, Weiss J (2012) Water absorption and critical degree of
605   saturation relating to freeze-thaw damage in concrete pavement joints. J Mater Civ Eng
606   24:299–307.

607   22. Cai H, Liu X (1998) Freeze-thaw durability of concrete: ice formation process in pores. Cem
608   Concr Res 28:1281–1287.

609   23. Li W, Sun W, Jiang J (2011) Damage of concrete experiencing flexural fatigue load and
610   closed freeze/thaw cycles simultaneously. Constr Build Mater 25:2604–2610.

611   24. Sun Z, Scherer GW (2010) Pore size and shape in mortar by thermoporometry. Cem Concr
612   Res 40:740–751.

613   25. Andersson K, Allard B, Bengtsson M, Magnusson B (1989) Chemical composition of cement
614   pore solutions. Cem Concr Res 19:327–332.

615   26. Pigeon M, Pleau R (2010) Durability of concrete in cold climates. CRC Press

616   27. Beddoe R, Setzer M (1988) A low-temperature DSC investigation of hardened cement paste
617   subjected to chloride action. Cem Concr Res 18:249–256.

618   28. Askeland DR, Pradeep PP (2003) The science and engineering of materials. Cengage
619   Learning

620   29. Debenedetti P (2003) Supercooled and glassy water. J. Phys. Condens. Matter 15.45 1669:

621   30. Wilding CR (1992) The performance of cement based systems. Cem Concr Res 22:299–310.

622   31. Qian Y, Farnam Y, Weiss J (2014) Using acoustic emission to quantify freeze–thaw Damage
623   of mortar saturated with naCl solutions. Proc. 4th Int. Conf. Durab. Concr. Struct. pp 32–37

624   32. Sun Z, Scherer GW (2010) Measurement and simulation of dendritic growth of ice in cement
625   paste. Cem Concr Res 40:1393–1402.

626   33. Thomas LC Heat transfer. Englewood Cliffs, N.J. : Prentice Hall

34. Velraj R, Seeniraj RV, Hafner B, et al. (1999) Heat transfer enhancement in a latent heat storage system. Sol Energy 65:171–180.

35. Lecomte D, Mayer D (1985) Design method for sizing a latent heat store/heat exchanger in a thermal system. Appl Energy 21:55–78.

36. Costa M, Buddhi D, Oliva A (1998) Numerical simulation of a latent heat thermal energy storage system with enhanced heat conduction. Energy Convers Manag 39:319–330.

37. Bentz D (2000) A computer model to predict the surface temperature and time-of-wetness of concrete pavements and bridge decks. US Department of Commerce, Technology Administration, National Institute of Standards and Technology.

38. Bentz DP, Turpin R (2007) Potential applications of phase change materials in concrete technology. Cem Concr Compos 29:527–532.

39. Zivkovic B, Fujii I (2001) An analysis of isothermal phase change of phase change material within rectangular and cylindrical containers. Sol Energy 70:51–61.

40. Ismail KAR, Abugderah MM (2000) Performance of a thermal storage system of the vertical tube type. Energy Convers Manag 41:1165–1190.

41. Hamada Y, Ohtsu W, Fukai J (2003) Thermal response in thermal energy storage material around heat transfer tubes: effect of additives on heat transfer rates. Sol Energy 75:317–328.

42. Voller VR, Swaminathan CR (1993) Treatment of discontinuous thermal conductivity in control-volume solutions of phase-change problems. Numer Heat Transf Part B Fundam 24:161–180.

43. Ismail KAR, Da Silva M das GE (2003) Numerical solution of the phase change problem around a horizontal cylinder in the presence of natural convection in the melt region. Int J Heat Mass Transf 46:1791–1799.

44. Fukai J, Hamada Y, Morozumi Y, Miyatake O (2003) Improvement of thermal characteristics of latent heat thermal energy storage units using carbon-fiber brushes: experiments and modeling. Int J Heat Mass Transf 46:4513–4525.

45. Gong Z-X, Mujumdar AS (1997) Finite-element analysis of cyclic heat transfer in a shell-and-tube latent heat energy storage exchanger. Appl Therm Eng 17:583–591.

46. Rubinsky B, Cravahlo EG (1981) A finite element method for the solution of one-dimensional phase change problems. Int J Heat Mass Transf 24:1987–1989.

47. Yoo J, Rubinsky B (2007) Numercial computation using finite elements for the moving interface in heat transfer problems with phase transformation. Numer Heat Transf 6:209–222.

48. Shamsundar N, Sparrow EM (1975) Analysis of multidimensional conduction phase change via the enthalpy model. J Heat Transfer 97:333.

49. Hibbert SE, Markatos NC, Voller VR (1988) Computer simulation of moving-interface, convective, phase-change processes. Int J Heat Mass Transf 31:1785–1795.

50. Smith WF, Hashemi J (2006) Foundations of materials science and engineering, 4th ed. McGraw-Hill

51. Callister WD, Rethwisch D (2009) Materials science and engineering: An introduction, 8th ed.

52. ASTM E1225-09. Standard Test Method for Thermal Conductivity of Solids by Means of the Guarded-Comparative-Longitudinal Heat Flow Technique. ASTM International, West Conhoshocken, PA

53. ASTM D5470-12: Standard Test Method for Thermal Transmission Properties of Thermally Conductive Electrical Insulation Materials 1.

54. Incropera FP, DeWitt DP, Bergman TL, Lavine AS (2007) Fundamentals of heat and mass transfer. John Wiley & Sons

55. Litvan G (1972) Phase transitions of adsorbates: IV, mechanism of frost action in hardened cement paste. J Am Ceram Soc 55:38–42.

56. Brun M, Lallemand A, Quinson J-F, Eyraud C (1977) A new method for the simultaneous determination of the size and shape of pores: the thermoporometry. Thermochim Acta 21:59–88.

57. Radlinska A, Rajabipour F, Bucher B, et al. (2008) Shrinkage mitigation strategies in cementitious systems: A closer look at differences in sealed and unsealed behavior. Transp Res Rec J Transp Res Board 2070:59–67.

58. Henkensiefken R, Bentz D, Nantung T, Weiss J (2009) Volume change and cracking in internally cured mixtures made with saturated lightweight aggregate under sealed and unsealed conditions. Cem Concr Compos 31:427–437.

59. Yang Z, Weiss WJ, Olek J (2006) Water transport in concrete famaged by tensile loading and freeze–thaw cycling. J Mater Civ Eng 18:424–434.

60. Sourirajan S, Kennedy GC (1962) The system H2O-NaCl at elevated temperatures and pressures. Am J Sci 260:115–141.

61. Levy O, Stroud D (1997) Maxwell Garnett theory for mixtures of anisotropic inclusions: Application to conducting polymers. Phys Rev B 56:8035–8046.

62. Progelhof RC, Throne JL, Ruetsch RR (1976) Methods for predicting the thermal conductivity of composite systems: A review. Polym Eng Sci 16:615–625.

63. Touloukian et al. (1970) Thermophysical properties of matter.

64. Hilsenrath et al. (1955) Tables of thermal properties of gases. NBS Circ. 564

65. Fletcher NH (2009) The Chemical Physics of Ice. Cambridge Univ. Press

66. Pitzer KS, Peiper JC, Busey RH (1984) Thermodynamic properties of aqueous sodium chloride solutions. J. Phys. Chem. Ref. Data 13:

67. Campbell-Allen D, Thorne CP (1963) The thermal conductivity of concrete. Mag Concr Res 15:39–48.

702 68. Daian J-F (1988) Condensation and isothermal water transfer in cement mortar Part I — Pore
703   size distribution, equilibrium water condensation and imbibition. Transp Porous Media
704   3:563–589.

705 69. Bentz D, Peltz M, Duran-Herrera A, et al. (2010) Thermal properties of high-volume fly ash
706   mortars and concretes. J Build Phys 34:263–275.

707 70. Zhou L-P, Wang B-X, Peng X-F, et al. (2010) On the Specific Heat Capacity of CuO
708   Nanofluid. Adv Mech Eng 2010:1–4.

709 71. Farnam Y, Esmaeeli HS, Bentz D, et al. (2015) Experimental and Numerical Investigation on
710   the Effect of Cooling/Heating Rate on the Freeze-Thaw Behavior of Mortar Containing
711   Deicing Salt Solution. Int. Conf. Regen. Conserv. Concr. Struct.

712 72. Farnam Y, Krafcik M, Liston L, et al. (2015) Evaluating the Use of Phase Change Materials
713   in Concrete Pavement to Melt Ice and Snow. J Mater Civ Eng 04015161.

714 73. Williams RJJ, Aldao CM (1983) Thermal conductivity of plastic foams. Polym Eng Sci
715   23:293–298.

716